Structure, magnetic properties and magnetoelastic anisotropy in epitaxial $Sr(Ti_{1-x}Co_x)O_3$ films

Structure, magnetic properties and magnetoelastic anisotropy in epitaxial $Sr(Ti_{1-x}Co_x)O_3$ films

Lei Bi, Hyun-Suk Kim, Gerald F Dionne[1] **and C A Ross**[2]

Department of Materials Science and Engineering, Massachusetts Institute of Technology Cambridge, MA 02139, USA
E-mail: caross@mit.edu

Abstract. We report the structure, magnetic properties and magnetoelastic anisotropy of epitaxial $Sr(Ti_{1-x}Co_x)O_3$ films grown on $LaAlO_3$ (001) and $SrTiO_3$ (001) substrates by pulsed laser deposition. Room temperature ferromagnetism was observed in the $Sr(Ti_{0.86}Co_{0.14})O_3$ and $Sr(Ti_{0.77}Co_{0.23})O_3$ films. The formation of magnetic secondary phases such as Co-metal clusters in $Sr(Ti_{0.77}Co_{0.23})O_3$ is excluded based on x-ray diffraction, cross-sectional TEM, x-ray photoelectron spectroscopy and x-ray-absorption near edge spectroscopy. A large magnetic anisotropy is observed in $Sr(Ti_{0.77}Co_{0.23})O_3$ films. The net anisotropy is strongly influenced by growth conditions and the substrate and is attributed to magnetoelastic effects. The magnetoelastic anisotropy is related to the valence and spin states of the Co ions, which contribute to the ferromagnetic properties. Magneto-optical characterization yields a figure of merit (Faraday rotation/optical absorption) of $0.57 \, deg \, dB^{-1}$ in the $Sr(Ti_{0.77}Co_{0.23})O_3$ film at 1550 nm wavelength, making it potentially useful in integrated magneto-optical applications.

[1] Also at MIT Lincoln Laboratory, Lexington, MA 02420, USA.
[2] Author to whom any correspondence should be addressed.

IOP Institute of Physics **Φ** DEUTSCHE PHYSIKALISCHE GESELLSCHAFT

Contents

1. Introduction

Magnetic semiconductors have attracted great interest since the first report of room-temperature ferromagnetism (RT-FM) in Co-doped TiO_2 films [1]. By introducing transition-metal ions into a diamagnetic host lattice, RT-FM and spin polarization can be achieved in these materials, making them very attractive for spintronic applications [2]. Meanwhile, high optical transparency and large magneto-optical response make these films also very attractive for fabricating integrated magneto-optical devices [3]. In the past decade, considerable research has been carried out on oxide films doped with 3d transition-metal ions, such as Cr- or Fe-doped In_2O_3 [4, 5], Co-doped ZnO [6, 7] and Co- or Fe-doped SnO_2 [8]. These films have proven to be dilute magnetic semiconductors with intrinsic RT-FM properties.

Among the oxide films, perovskite-structured $SrTiO_3$ shows good silicon compatibility [9] and excellent optical transparency at communication wavelengths [10], making it a promising candidate material for spintronic and integrated magneto-optical applications provided RT-FM can be achieved by doping. Zhang *et al* [11] studied 2 at.% Co-doped $Nb : SrTiO_3$ thin films but no RT-FM was observed. On the other hand, Co-doped $(La, Sr)TiO_3$ shows RT-FM [12]–[14], but the origin of ferromagnetism is still under debate. Recently, $Sr(Ti_{1-x}Fe_x)O_3$ [15] and Co-doped $BaTiO_3$ films [16] showed RT-FM behavior. Meanwhile, $Sr(Ti_{1-x}Co_x)O_3$ bulk samples [17, 18] show paramagnetic or spin-glass behavior with no RT-FM for any Co concentration. The differences between bulk and thin film materials may be caused by different valence states of Co in bulk compared to thin films [18]. Co valence states may be varied by changing the oxygen partial pressure and, consequently, the oxygen stoichiometry during growth. Lattice strains in epitaxial films can also change the film properties compared to bulk materials. There is therefore a need for a systematic analysis of the film structure and magnetic properties to understand the origin of RT-FM in 3d transition metal ion-doped perovskite–structured films. In this study, we report the RT-FM properties, magnetic anisotropy and magneto-optical properties of $Sr(Ti_{1-x}Co_x)O_3$ films. Epitaxial $Sr(Ti_{1-x}Co_x)O_3$ films were grown on $SrTiO_3$ (cubic, $a = 3.905$ Å at room temperature) and $LaAlO_3$ (rhombohedral below $435\,^\circ$C, $a = b = 5.365$ Å, $c = 13.11$ Å (expressed in hexagonal geometry), a (pseudo-cubic) $= 3.79$ Å at room temperature) substrates to study the magnetic anisotropy dependence on substrate lattice parameters. It was found that RT-FM and strong magnetic anisotropy can be achieved in $Sr(Ti_{0.86}Co_{0.14})O_3$ and $Sr(Ti_{0.77}Co_{0.23})O_3$ films fabricated under high vacuum. From our detailed structural and property characterizations, we exclude the possibility of Co metal clusters as a major contributor to the ferromagnetic properties. The magnetoelastic anisotropy in these films may provide evidence for the valence state of the Co ions contributing to the RT-FM properties.

2. Experimental methods

$Sr(Ti_{1-x}Co_x)O_3$ films were epitaxially grown on $LaAlO_3$ (001) (LAO) substrates by pulsed laser deposition (PLD) from single phase $Sr(Ti_{1-x}Co_x)O_3$ targets with $x = 0.05$, 0.1, 0.2, 0.3 and 0.5. The films are named STC5, STC10, STC20, STC30 and STC50, respectively. Several samples were also deposited on $SrTiO_3$ (001) (STO) substrates for comparison. The targets were made by standard ceramic fabrication processing. A coherent COMPexPro 205 KrF (248 nm) excimer laser was used for thin film fabrication. The pulse frequency was 10 Hz and the fluence was about $2.5\,J\,cm^{-2}$. The film deposition rate was around $5\,nm\,min^{-1}$. During deposition, the substrates were kept at $700\,°C$ and the chamber was kept in vacuum with a pressure of typically 3.0×10^{-6} Torr [15]. For comparison, several STC30 samples were grown under different pressures ranging from 2.5×10^{-6} to 3.5×10^{-6} Torr on LAO substrates. The target-to-substrate distance was kept at 5.5 cm for all samples. The typical film thickness was 300 nm as determined by a profilometer. The composition of the STC5, STC20, STC30 and STC50 films was measured by wavelength dispersive x-ray spectrometry (WDS) to be $Sr(Ti_{0.93}Co_{0.07})O_3$, $Sr(Ti_{0.86}Co_{0.14})O_3$, $Sr(Ti_{0.77}Co_{0.23})O_3$ and $Sr(Ti_{0.63}Co_{0.37})O_3$, respectively. Based on the ionic radii (Sr^{2+}: 132pm, Co^{2+}: 84pm, Co^{3+}: 72pm, Co^{4+} high spin: 67pm, Ti^{4+}: 68pm), we expect the Co to be in the B sites. Both conventional one-dimensional x-ray diffraction (1DXRD) and two-dimensional x-ray diffraction (2DXRD) were carried out to characterize the structure of the films. The reciprocal space map (RSM) was also measured on STC30 to determine the film's in-plane lattice parameter and the strain state. Cross-sectional TEM imaging was performed on STC30. Energy dispersive spectroscopy (EDS) mapping using the Co K line in scanning transmission electron microscopy (STEM) mode was performed along the film thickness direction to evaluate the homogeneity of the Co distribution. X-ray photoelectron spectroscopy (XPS) was measured on a Kratos Axis Ultra spectrometer with a monochromated Al K_α source and a hemispherical analyzer. The high-resolution spectrum at the Co K-edge was measured with a pass energy of 20 eV and an energy resolution of 0.3 eV. X-ray absorption near edge spectroscopy (XANES) at the Co K-edge was also carried out to determine the Co valence state in the STC30 film. The measurement was performed in fluorescence mode at beamline U7C of the National Synchrotron Radiation Facility, China. The electron-beam energy was 0.8 GeV, and the maximum stored current was about 250 mA. A water-cooled Si(111) plane double crystal monochromator was used. As a comparison, the XANES spectrum of a Co metal sample at the Co K-edge was also measured on the same beamline. Room temperature out-of-plane (OP) and in-plane (IP) magnetic hysteresis were measured by a vibrating sample magnetometer (VSM). Temperature-dependent magnetization curves were measured on STC30 between 5 and 1000 K both by a superconducting quantum interference device (SQUID) and a VSM. The Faraday rotations of all films were characterized on a custom-built apparatus at 1550 nm wavelength, with the laser light and magnetic field directions perpendicular to the film plane [19]. Optical transmission spectra of the STC films were characterized by UV–Vis–(NIR) near-infrared spectrophotometry with a wavelength range of 175–2000 nm. The optical constants (the refractive index n and extinction coefficient k) were also characterized from 400 to 1700 nm wavelength for an STC30 film on a WVASE32 ellipsometer. General oscillator models were applied to fit the optical constants, and the fitting root mean square error was smaller than 1.
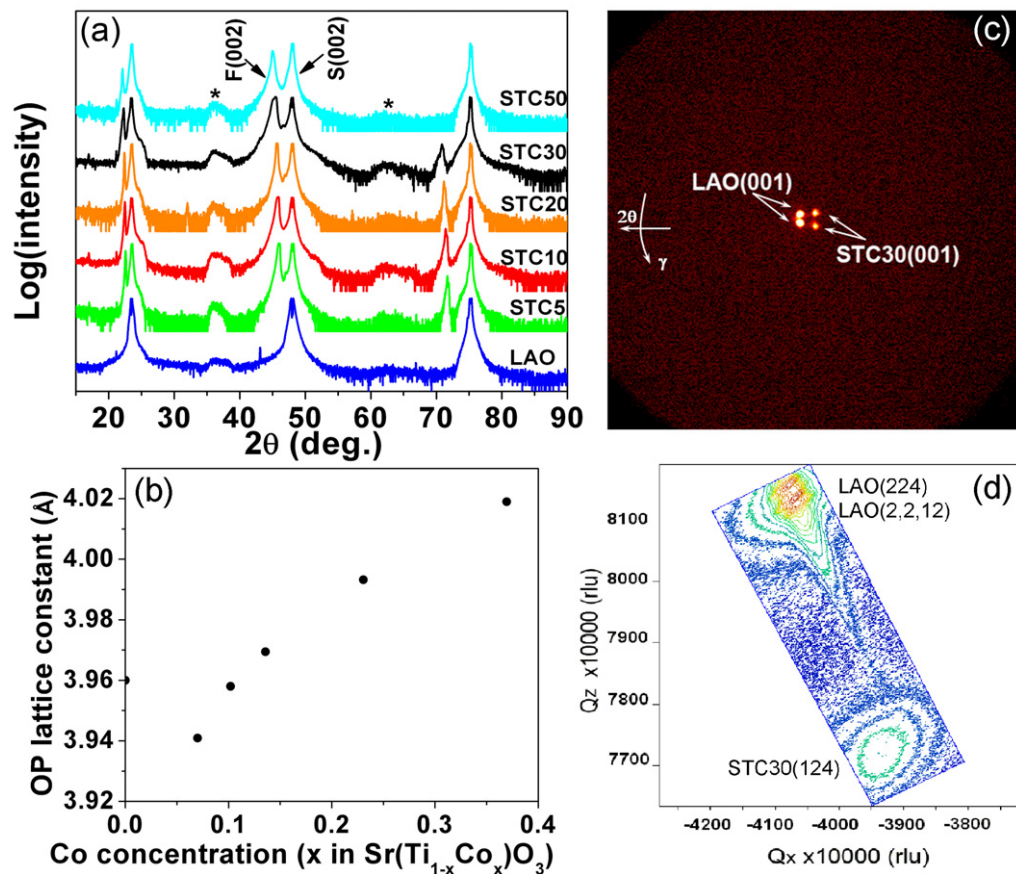
Figure 1. (a) 1DXRD θ–2θ scans for a bare LAO substrate and STC films with various Co concentrations. F(002) and S(002) indicate one of the (00l) diffraction peaks of the film and the substrate, respectively. The broad diffraction features marked by '∗' arise from the twin defects of the LAO substrates. (b) OP lattice parameter of STC films as a function of Co concentration determined by the STC(00l) diffractions. The measurement error is within the size of the symbols. (The data point around 10 at.% is an interpolation to the measurement data of the other samples.) (c) 2DXRD diffraction pattern of STC30 film taken at an x-ray incident angle of $\theta = 11.5°$. The frame center was $2\theta = 23°$. The data collection region is $8° \leqslant 2\theta \leqslant 38°$ and $-15° \leqslant \gamma \leqslant 15°$. The sample was rotated by $360°$ about the axis normal to the sample surface during the measurement. (d) RSM of the STC30 film (124) and the LAO substrate (244) and (2,2,12) diffraction patterns (both $K_{\alpha 1}$ and $K_{\alpha 2}$ peaks). Rlu stands for the reciprocal space unit. 1 rlu $= 2/\lambda$, where λ is the wavelength of the Cu $K_{\alpha 1}$ line, 0.154056 nm. The film is epitaxially grown on the substrate at 3.0×10^{-6} Torr and is in a state of IP compressive stress.

3. Results and discussion

Figure 1(a) shows the 1DXRD $\theta - 2\theta$ scan spectra of the STC films grown on LAO substrates. Except for STC20, which additionally shows weak polycrystalline diffraction peaks from the STC(111) and STC(211) planes (about 2 orders of magnitude weaker than the single-crystal

peak), all the other films show only STC(00*l*) diffraction peaks, indicating a 'cube-on-cube' orientation relation between the film and the substrate. The broad diffraction features marked by '∗' are from twin defects in the LAO substrates. Such features are not observed for films grown on STO substrates under similar fabrication conditions. There are no diffraction peaks from secondary phases observed in any of the films. The calculated OP lattice parameter of the STC films based on the (00*l*) diffraction peaks is shown in figure 1(b). The OP lattice constant of STC increases from 3.94 to 4.02 Å as the Co concentration increases from 7 to –37 at.%, which indicates that the Co is incorporated substitutionally into the STC lattice. As a comparison, the OP lattice constant of SrTiO$_3$ fabricated under similar conditions is 3.96 Å. In contrast, in STC bulk samples, the lattice constant *decreases* linearly with increasing Co concentration up to 90% Co at the Ti site [17, 18]. The inverse trend observed here may suggest that the Co ions in the films are in lower valence states than in bulk samples, so that the lattice expands with increasing Co concentration instead of contracting. This observation will be supported by our XPS characterization results given below. Figure 1(c) shows the 2DXRD spectrum of the STC30 film. The well-defined spot-like diffraction pattern of the STC (001) planes suggests epitaxial growth of the STC30 film. The epitaxial growth of STC30 on LAO is further indicated by the spot-like STC30 (124), LAO (244) and LAO (2,2,12) diffraction patterns in the x-ray RSM as shown in figure 1(d). Q_x and Q_z correspond to reciprocal spacings along the STC30 [020] IP direction and the STC30 [004] OP direction, respectively. The difference between the Q_x values of the film and substrate diffraction spots indicates that the lattice mismatch strain is partially relaxed by misfit dislocations during growth. The OP and IP lattice parameters of the film were 3.993 and 3.914 Å, respectively, both of which are larger than the substrate lattice constant, 3.786 Å. Considering that bulk STC samples show cubic symmetry [17, 18], the unit cell of the STC30 film grown on the LAO substrate is rendered tetragonal and the film shows IP compressive stress.

A cross-sectional TEM image of an STC30 film on an LAO substrate is shown in figure 2(a). The film and the substrate show a semi-coherent interface (a misfit dislocation is visible), and no clusters or secondary phases were found in the film. The inset shows the diffraction pattern at the interface region, which has no evidence of secondary phases. We checked the homogeneity of the STC lattice at various locations in the film. As shown in figure 2(b), a uniform perovskite lattice was observed over large areas in the STC film. The two arrows indicate two structural defects in the film, which are likely to be misfit dislocations or twin boundaries. This observation is consistent with the partially strain relaxed epitaxial growth scenario as suggested by the x-ray RSM. The inset of figure 2(b) shows the EDS mapping of Co within the film cross-section. The Co is distributed homogeneously, and there is no Co-rich region along the interface.

The valence state of Co ions in the STC30 film was characterized by XPS and XANES. Figure 3(a) shows the XPS core-level spectra of Co 2p in STC30. The two peaks located at binding energies of 780.4 and 796.2 eV are the Co 2p$_{3/2}$ and 2p$_{1/2}$ doublets arising from spin–orbital interaction. In contrast, Co metal has Co 2p$_{3/2}$ and 2p$_{1/2}$ at 777.3 and 792.4 eV, respectively [20]. This difference precludes the existence of Co metal at the STC film surface. Two strong satellite peaks were observed at around 7 eV above the principal peaks. The binding energy separation between the principal and satellite peaks is comparable with that of Co^{2+} or Co^{3+} ions in previous reports [20]–[23]. The observation of strong satellite peaks is characteristic of high-spin Co^{2+} [20], as seen in a Co^{2+}-containing layered perovskite La$_2$CoO$_4$ [24], compared to the very weak satellite peaks observed for Co^{3+} and Co^{4+} ions in
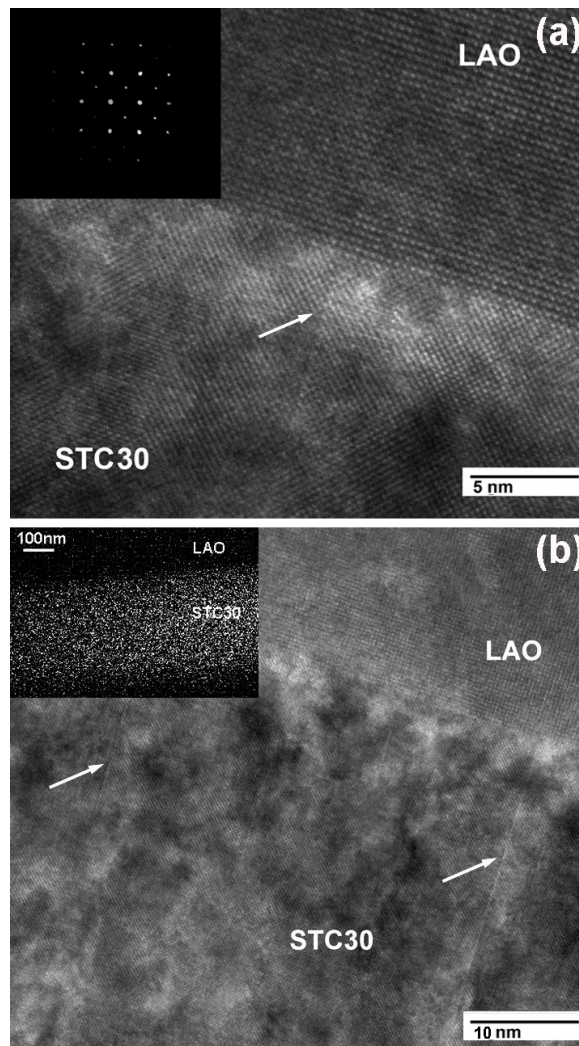
Figure 2. (a) Cross-sectional TEM image of the STC30/LAO sample. The inset shows the diffraction pattern at the interface region. (b) Cross-sectional TEM image of the same sample showing a large area homogeneity of the perovskite lattice with two dislocations marked by arrows. The inset shows the EDS mapping of Co distribution in the film cross section.

$La_{1-x}Sr_xCoO_3$ [26] or STC bulk samples [17] fabricated under high oxygen pressure. Therefore, the strong satellite peak in our XPS spectrum indicates that Co^{2+} is present in the STC lattice. However, the binding energy of the Co $2p_{3/2}$ peak is smaller than that of pure Co^{2+} perovskites (781.3 eV) [24], suggesting that Co is in a mixed valence state also containing Co^{3+} and Co^{4+}. The amounts of each type of Co ion will be determined by the oxygen stoichiometry, which was not measured here, but in comparison, $SrTiO_3$ films fabricated under a similar high vacuum had a formula of $SrTiO_{2.5}$ [25]. A similar oxygen stoichiometry in the STC films would imply significant amounts of Co^{2+} and Co^{3+} to maintain charge balance. Quantitative analysis of the relative concentration of Co is difficult due to the lack of standard XPS spectra. However, based on the measured XPS spectra of Co in $LaCoO_3$, $SrCoO_3$ and La_2CoO_4, we estimate that Co^{2+} and Co^{3+} are the major valence states of Co. The lower valence state of Co ions in the STC film
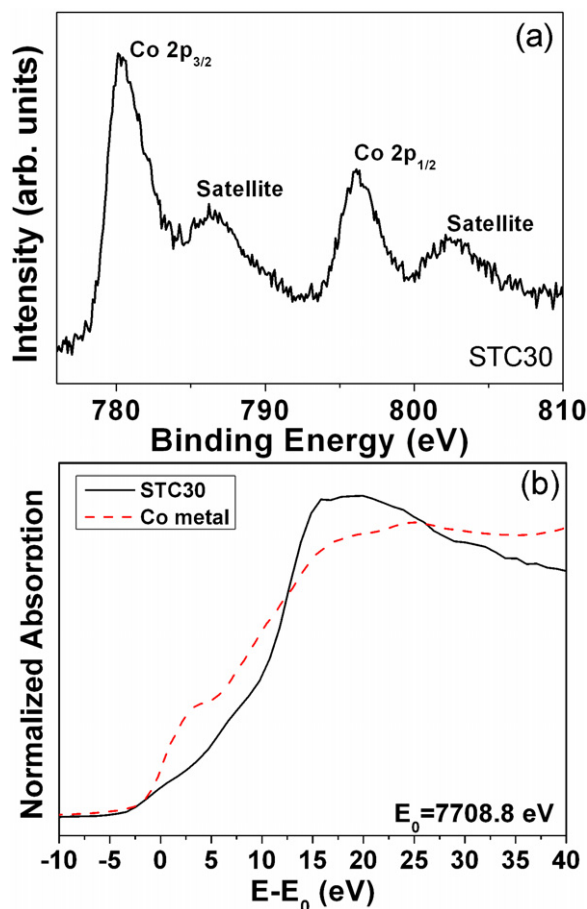
Figure 3. (a) XPS spectrum of the Co 2p peaks in STC30. (b) Co K-edge XANES spectrum of the STC30 film with Co metal as a reference sample.

compared with STC bulk samples is attributed to the low oxygen partial pressure used in film deposition. A low valence state yields a larger average diameter of the Co ions, and the STC lattice therefore expands with increasing Co concentration, as illustrated in figure 1(b).

Although XPS provides information on the valence states of Co ions, it only measures the surface layer (~ 5 nm) of the STC film. In order to understand the Co valence states and local environments over a larger sampling depth, fluorescence yield mode XANES at the Co K-edge was carried out for the STC30 film, as shown in figure 3(b). For comparison, the Co metal absorption spectrum is also shown in the figure. An absorption plateau at $E-E_0 = 3$ eV is a fingerprint for Co metal clusters [7, 27]. This feature was not observed in the STC30 film. In a previous report by Kasper *et al* [27] in a dilute Co-doped TiO_2 system, 13% Co atoms in the metallic state produced a clear absorption plateau structure at $E-E_0 = 3$ eV. We compared the STC30 spectrum pre-edge feature with calculated spectra based on mixtures of CoO and Co and confirmed that the metallic cobalt atom concentration in the STC30 film is at most a few per cent. There are other notable features in the XANES spectrum. The absorption threshold energy of Co in STC30 is much higher than that of Co metal, indicating the Co ions are substituting for Ti and are located in an oxygen octahedron. The absorption spectrum rises slowly and continuously at E_0 rather than sharply increasing with a plateau structure as found for Co metal.
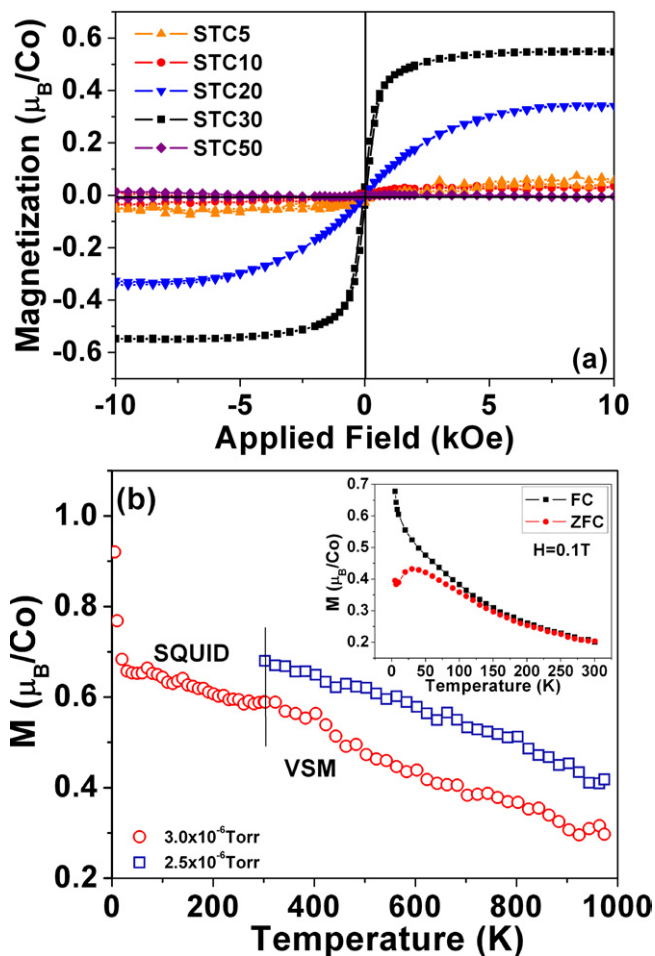
Figure 4. (a) Room temperature OP magnetic moment of STC samples on LAO substrates. Only STC20 and STC30 samples showed clear RT-FM hysteresis. (b) The saturation magnetic moment versus temperature curve of two samples of STC30 measured at 8000 Oe with the magnetic field applied OP. The inset shows the FC and ZFC magnetic moments of the STC30 film grown at 3×10^{-6} Torr under an IP applied field of 1000 Oe.

This feature resembles the simulation results of Co-doped TiO_2-containing oxygen vacancies besides the Co_{Ti} sites [28], in which Co ions also occupy an oxygen octahedron. An enhanced absorption tail was also observed in the Cr K-edge XANES spectrum of Cr-doped $SrTiO_3$ with a high oxygen vacancy concentration [29], which was explained by the increase of the density of states of the Cr 4p level by nearby oxygen vacancies at the Cr 4p band edge. Comparing with these reports, the XANES spectrum for the STC30 film suggests that the Co ions are substituting for the Ti ions in the STC lattice with oxygen vacancies present at neighboring sites.

Figure 4(a) shows the OP magnetic hysteresis loops of STC films grown on LAO substrates at room temperature. The hysteresis loops were obtained by subtracting the diamagnetic signal from the LAO substrates. All the samples were grown at a vacuum level of 3.0×10^{-6} Torr. When the Co concentration is low, the films show no significant RT-FM behavior, which is consistent with a previous report [11]. However, with increasing Co concentration, STC20 and
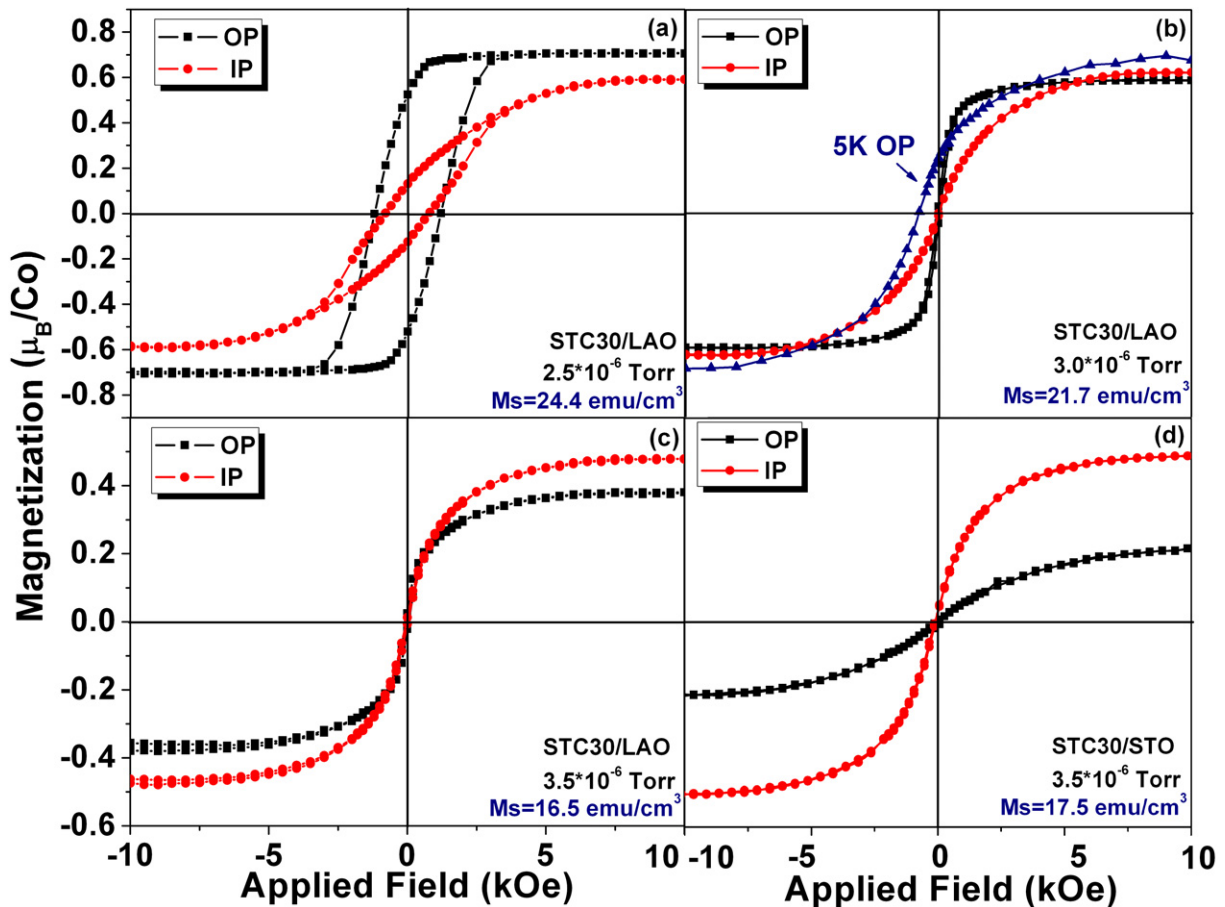
Figure 5. (a)–(c) Magnetic hysteresis showing different saturation magnetic moment, coercivity and anisotropy for STC30 samples grown on the LAO substrates under different conditions noted in the plots. Also shown is the low-temperature half-hysteresis loop measured from -1 to $1\,\mathrm{T}$ at $5\,\mathrm{K}$ for STC30 sample grown at $3.0 \times 10^{-6}\,\mathrm{Torr}$, which shows a clear ferromagnetic behavior. (d) Magnetic hysteresis for STC30 grown on an STO substrate. A background signal corresponding to a bare substrate was subtracted.

STC30 show clear magnetic hysteresis with a saturation magnetization of 0.34 and 0.55 $\mu_\mathrm{B}\,\mathrm{Co}^{-1}$ (equivalent to 9.30 and 21.60 emu cm^{-3}, respectively). The OP coercivities of STC20 and STC30 are 32 and 40 Oe, respectively. At 5 K, the coercivity of STC30 increases to ~ 800 Oe and shows a clear ferromagnetic hysteresis as seen in figure 5(b). Further increasing the Co concentration resulted in a decrease of the magnetic moment. Almost no RT-FM behavior was found for STC50, which may be attributed to increased populations of antiferromagnetically superexchange-coupled Co ions in high concentrations.

The OP saturation magnetization versus temperature curve of the STC30 film on LAO measured at 8000 Oe is shown in figure 4(b). A Curie temperature higher than 1000 K was found for the film. At $T < 20\,\mathrm{K}$, a sharp upturn of the M_s with decreasing temperature was observed, which is believed to be a Brillioun–Weiss curve originating from paramagnetic Co ions. At $T > 20\,\mathrm{K}$, the M_s decreases almost linearly with increasing T, deviating from both the

Curie–Weiss law and the Brillouin–Weiss equation. Such a linear M_s–T curve with a similar slope is also observed in another STC30 sample grown at a lower base pressure of 2.5×10^{-6} Torr as shown in figure 4(b). The inset shows the field cooling (FC) and zero-field cooling (ZFC) curves of the sample grown at 3×10^{-6} Torr measured with an IP magnetic field of 1000 Oe. The thermomagnetic irreversibility between the FC and ZFC curves indicates a spin glass or superparamagnetic behavior. These findings provide further evidence related to the possibility of Co metal clusters in the STC films. If the ferromagnetism were from Co metal clusters, the temperature at the maximum magnetization of the ZFC curve (~ 40 K in this case) would be the blocking temperature T_B. The Co cluster size can be estimated using $K_A V = 25 \, k_B T_B$, [30] where K_A is the magnetic anisotropy constant ($K_A \sim 4.5 \times 10^6$ ergs cm^{-3} for Co metal), k_B is the Boltzmann constant and V is the particle volume. Substituting T_B into this equation yields an average Co cluster size of $V = 31$ nm^3 (diameter $D \sim 3.85$ nm). Co clusters in this size range would have been clearly visible in our cross sectional TEM images. Indeed, considering that Co metal has a saturation magnetization value of $1.7 \, \mu_B$ Co^{-1}, from the saturation magnetization of the sample at 20 K ($0.68 \, \mu_B$ Co^{-1}), we estimate that sixteen 3.85 nm diameter Co metal clusters on average should show up in the sampling region in figure 2(b) if all the ferromagnetic signal originated from Co metal clusters, assuming the HRTEM sample thickness is only 10 nm. The probability of missing all these nanoclusters in the HRTEM image is 1×10^{-7}. Additionally, the STC30 film magnetization of $0.68 \, \mu_B$ Co^{-1} implies that if the magnetism had come from metallic Co, about 40% of the Co would be metallic, which would have shown up in the XANES spectrum [27]. These results indicate that the RT-FM property observed in the STC30 sample is not due to Co metal clusters in the film. Recently, thermomagnetic irreversibility has been reported in structurally homogeneous Sr(Ti$_{1-x}$Fe$_x$)O$_3$ [12], Co-doped BaTiO$_3$ [13], BaFe$_{1-x}$Zr$_x$O$_3$ [31] and Co-doped TiO$_2$ films [32]. A mixed-state ferromagnetism scenario has been proposed in Co-doped TiO$_2$ [32], in which Co still resides in the rutile lattice site but exchange coupling between Co$_{Ti}$–Co$_{interstitial}$ or neighboring Co$_{Ti}$–Co$_{Ti}$ pairs leads to ferromagnetism. In STC films, mixed valence is confirmed by XPS, and this may lead to spin-glass behavior (and the associated thermomagnetic irreversibility) as found in bulk STC [17].

In order to understand the origin of ferromagnetism in the STC films, we deposited STC30 under various conditions and on both LAO and STO substrates. STC30 grown on LAO substrates shows different saturation magnetization, coercivity and magnetic anisotropy depending on the deposition base pressure and growth rate. From figures 5(a)–(c), a general finding is that lower deposition pressure yields higher saturation magnetization (M_s) and coercivity (H_c), which are associated with a stronger OP anisotropy for films grown on LAO substrates. (A small IP anisotropy may appear upon cooling below 435 °C for films grown on LAO substrates during the substrate structure transition from cubic to rhombohedral. This effect is expected to be minor compared to the strong OP anisotropy found in these films.) As the base pressure is increased from 2.5×10^{-6} to 3.5×10^{-6} Torr, the M_s decreases from 24.4 to 16.5 emu cm^{-3}, H_c (OP) decreases from 1200 Oe to almost zero and the film anisotropy changes from highly OP to almost isotropic. These observations suggest that oxygen vacancies play an important role in determining the valence states of the Co ions and the overall magnetic properties of the film. Higher oxygen vacancy concentrations yield stronger ferromagnetic behavior of the STC films, and the associated changes of Co valence and spin state may be responsible for changes in the magnetic anisotropy. Measurements along different IP crystallographic directions indicated no measurable IP anisotropy.

The magnetic anisotropy in the film is attributed to a magnetoelastic effect with Co ions showing a positive magnetostrictive constant along the [001] (OP) direction. Further evidence for magnetoelastic effects is provided by figure 5(d), which shows magnetic hysteresis of STC30 deposited on an STO substrate. STO has a larger lattice constant (3.905 Å) than LAO (3.786 Å), resulting in a much smaller compressive stress in the STC30 (lattice mismatch <1%) and the STC has an IP easy magnetization plane, which is opposite to the behavior seen in figures 5(a) and (b). Since all the STC30 films are (100) oriented and have similar geometries, these changes in magnetic anisotropy cannot be explained by shape or crystalline anisotropies, but are consistent with magnetoelastic effects in the strained STC films.

The observed OP 'easy' axis anisotropy in compressively strained films on LAO illustrated dramatically in figure 5(a) invites speculation about the valence and spin state of the Co ions that contribute to the anisotropic magnetization properties. Co^0 (Co metal clusters) showed almost no magnetic anisotropy in Co-doped TiO_2 [33]. Except for the case of ideal stoichiometry where only Co^{4+} ($3d^5$ low-spin $t_{2g}^5 e_g^0$ with $S = 1/2$) can replace diamagnetic Ti^{4+} in the octahedral B sites of the STC film, O^{2-} anion depletion that occurs during deposition under partial vacuum will allow the formation of reduced valence Co^{3+} ($3d^6$ low-spin $t_{2g}^6 e_g^0$ with $S = 0$) and Co^{2+} ($3d^7$ high-spin $t_{2g}^5 e_g^2$ with $S = 3/2$). The multi-valence condition is also discussed in the interpretation of the XPS spectrum. If it is assumed that local spin pairing among Co^{2+} ions by antiferromagnetic superexchange is not significant at these concentrations, the maximum effective magnetic moment in μ_B per Co ion would be limited by the average of the three spin values weighted by their population fractions, as fixed by the concentration of O^{2-} vacancies. Because Co^{4+} and Co^{2+} have similar degenerate states in the t_{2g} shell, both have unquenched orbital angular momentum with spin–orbit coupling that renders them strongly magnetoelastic [34, 35]. This situation can account for the observed magnetocrystalline anisotropy effects in the curves of figure 5. In addition, the influence of external stress on the magnetization process has long been important in shaping hysteresis loops of bulk ferrites and is particularly evident in films at the interface with the substrate where lattice mismatches occur [36]–[38]. As a consequence, it is appropriate to consider the various valence/spin-configuration combinations that might favor the OP easy axis observed in figure 5.

For strain conditions that produce an OP easy axis where the local site symmetry is tetragonal, the OP anisotropy can be the result of $Co^{4+} t_{2g}^5 e_g^0$ (LS) either spontaneously or from a strain-induced stabilization of the unpaired spin, and also from $Co^{2+} t_{2g}^5 e_g^2$ (HS) ions that feature a singlet ground state compatible with a positive Jahn–Teller magnetostriction effect ($\lambda_{100} > 0$) in the t_{2g} shell [35, 38]. These models are illustrated in figure 6. In ligand field theory, the 10 Dq value indicates the separation of the e_g and t_{2g} levels (shown by dashed lines) of a transition metal ion in octahedral O_h symmetry. In a strained tetragonalized octahedron, the e_g and t_{2g} levels (shown by solid lines) become non-degenerate and deviate from their original values. For our STC30 films deposited on LAO substrates, the CoO_6 octahedron undergoes a highly tetragonal z-axis expansion induced by IP compressive stress as confirmed by x-ray RSM measurements. The e_g doublet and t_{2g} triplet states separated by 10 Dq in the main cubic component of the site crystal field then split further. Specifically, under biaxial compressive stress in the $x - y$ plane, orbital states of the lower t_{2g} group are split by δ_t into a ground doublet (d_{xz}, d_{yz}) and an excited d_{xy} singlet; the e_g doublet splits by δ_e into lower d_{z^2} and higher $d_{x^2-y^2}$ singlet states. Such configurations correspond to the $Co^{4+} t_{2g}^5 e_g^0$ (LS) and $Co^{2+} t_{2g}^5 e_g^2$ (HS) ions that undergo Jahn–Teller z-axis expansions enhanced by IP compressive strain according to Poisson's ratio.
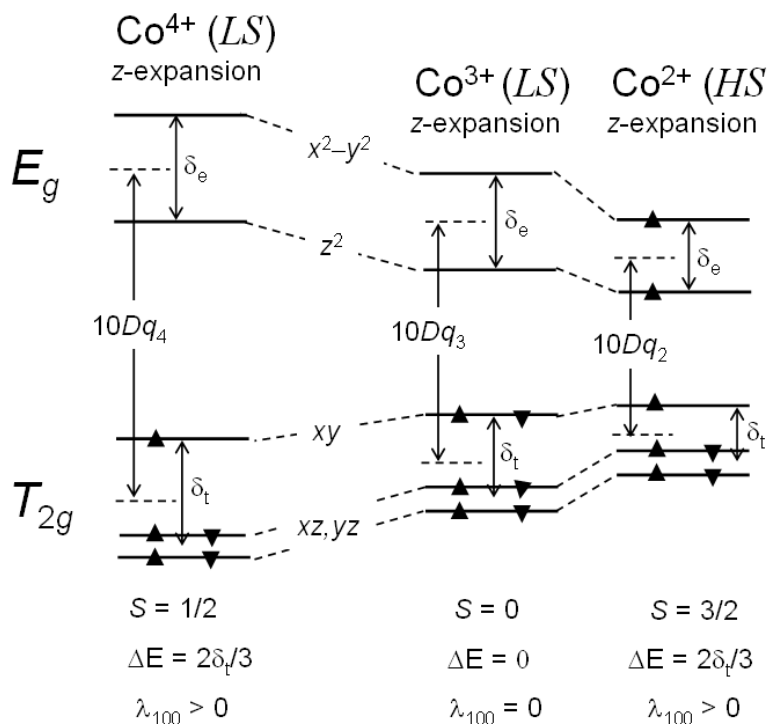
Figure 6. Orbital energy level diagrams for a tetragonally distorted octahedral site with spin occupancies of Co^{4+} (LS), Co^{3+} (LS) and Co^{2+} (HS) ions in STC30 films grown on $LaAlO_3$ substrates.

For films deposited on STO substrates, the much smaller IP compressive stress can allow the tetragonal splittings to invert, thereby reversing the signs of δ_t and δ_e to produce a negative λ_{100} and create ground-state doublets that can allow further stabilization by spin–orbit coupling [35]. The systematic changes of the magnetoelastic anisotropy for STC on LAO shown in figures 5(a)–(c) may also indicate that the Co valence and spin states are sensitive to fabrication conditions. Characterization of the Co spin states in future studies would provide more information to support this model.

Figure 7(a) shows the Faraday rotation of STC films grown on LAO substrates measured at 1550 nm wavelength. The Faraday rotation spectrum resembles the OP magnetic hysteresis shown in figure 4(a), although the Faraday coercivity is larger, 370 Oe for STC30. This result is similar to our previous report on Co-doped CeO_2, and may be related to the excitation state of the electric dipole transitions, which cause Faraday rotation [39]. An optical transmission measurement of STC films by UV–Vis–NIR spectrophotometry is shown in figure 7(b). The optical band gap for STC30 is 4.15 eV, which is about 0.25 eV higher than pure $SrTiO_3$ fabricated under similar conditions. With increasing Co concentration, the optical transmittance of STC films increases at visible to NIR wavelength ranges. Such behavior is similar to that of $Sr(Ti_{1-x}Fe_x)O_3$ films [15]. Co^{2+} and Co^{3+} ions at Ti sites behave as acceptors, while oxygen vacancies behave as donors. As Co content increases, free carrier density and optical absorption in the film decrease. The surface resistivity of STC films measured by the Van der Pauw method is shown in the inset of figure 7(b). With increasing Co concentration, the film changes from a semiconductor (STC0) to an insulator (STC30 and STC50), suggesting a non-carrier-mediated
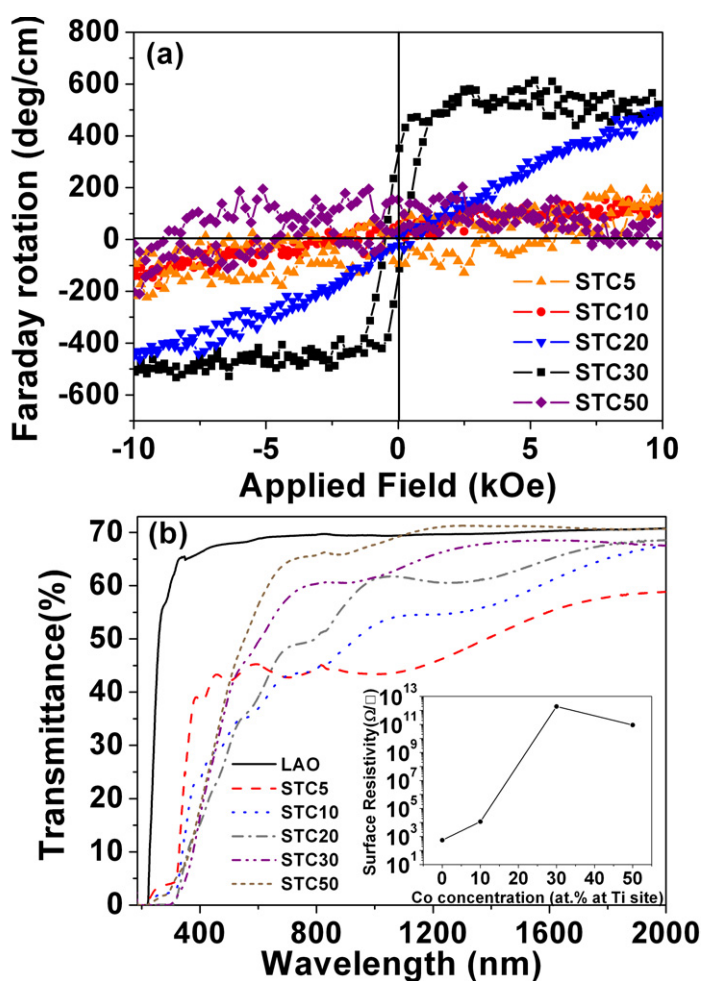
Figure 7. (a) Room temperature Faraday rotation of STC samples at 1550 nm wavelength, measured OP. (b) The optical transmission spectra of STC films grown on LAO with a bare LAO substrate as a reference sample. The inset shows the surface resistivity as a function of Co concentration for several STC films.

mechanism in ferromagnetic STC30. Hall measurements indicate a negatively charged carrier density of 2.8×10^{20} cm^{-3} in STC0, suggesting a significant concentration of oxygen vacancies in films fabricated under high vacuum. The other films were too resistive to inject sufficient current for Hall measurements. The systematic resistant change of the films supports the defect chemistry model discussed above.

The optical constants of STC30 films were also characterized by ellipsometry. The film shows an extinction coefficient of low 10^{-3} value at NIR wavelengths. A figure of merit (Faraday rotation divided by absorption loss) of 0.57 deg dB^{-1} is estimated in STC30 films at 1550 nm wavelength, which may be useful in integrated magneto-optical applications.

4. Summary and conclusions

Epitaxial $Sr(Ti_{1-x}Co_x)O_3$ films were fabricated by PLD on $LaAlO_3(001)$ and $SrTiO_3(001)$ substrates. RT-FM with a high Curie temperature and strong magnetic anisotropy were observed

in the STC20 ($x = 0.14$) and STC30 ($x = 0.23$) samples. Co ions substitute at the Ti site of the STC lattice, and there is no evidence of Co metal clusters. Significant magnetic anisotropy is observed in STC30 epitaxial films depending on fabrication conditions and substrate type. The magnetic anisotropy is attributed to magnetoelastic effects in the strained films and is related to the valence and spin states of the Co ions contributing to the RT-FM property. Magneto-optical characterization of STC30 shows a figure of merit of $0.57 \deg dB^{-1}$ at $1550 \, nm$ wavelength, suggesting that it may be useful in integrated magnetooptical device applications.

Acknowledgments

References

[1] Matsumoto Y, Murakami M, Shono T, Hasegawa T, Fukumura T, Kawasaki M, Ahmet P, Chikyow T, Koshihara S and Koinuma H 2001 *Science* **291** 854
[2] Žutić I, Fabian J and Sarma S D 2004 *Rev. Mod. Phys.* **76** 323
[3] Pacuski W, Ferrand D, Cibert J, Deparis C, Gaj J A, Kossacki P and Morhain C 2006 *Phys. Rev.* B **73** 035214
[4] Philip J, Punnoose A, Kim B I, Reddy K M, Layne S, Holmes J O, Satpati B, Leclair P R, Santos T S and Moodera J S 2006 *Nat. Mater.* **5** 298
[5] Yoo Y K *et al* 2005 *Appl. Phys. Lett.* **86** 042506
[6] Ueda K, Tabata H and Kawai T 2001 *Appl. Phys. Lett.* **79** 988
[7] Song C, Geng K W, Zeng F, Wang X B, Shen Y X, Pan F, Xie Y N, Liu T, Zhou H T and Fan Z 2006 *Phys. Rev.* B **73** 024405
[8] Kim H S, Bi L, Dionne G F, Ross C A and Paik H J 2008 *Phys. Rev.* B **77** 214436
[9] McKee R A, Walker F J and Chisholm M F 1998 *Phys. Rev. Lett.* **81** 3014
[10] Gaidi M, Stafford L, Margot J, Chaker M, Morandotti R and Kulishov M 2005 *Appl. Phys. Lett.* **86** 21106
[11] Zhang S X, Ogale S B, Kundaliya D C, Fu L F, Browning N D, Dhar S, Ramadan W, Higgins J S, Greene R L and Venkatesan T 2006 *Appl. Phys. Lett.* **89** 012501
[12] Herranz G *et al* 2006 *Phys. Rev. Lett.* **96** 027207
[13] Zhang S X *et al* 2007 *Phys. Rev.* B **76** 085323
[14] Zhao Y G *et al* 2003 *Appl. Phys. Lett.* **83** 2199
[15] Kim H S, Bi L, Dionne G F and Ross C A 2008 *Appl. Phys. Lett.* **93** 092506
[16] Lin Y H, Zhang S Y, Deng C Y, Zhang Y, Wang X H and Nan C W 2008 *Appl. Phys. Lett.* **92** 112501
[17] Malo S and Maignan A 2004 *Inorg. Chem.* **43** 8169
[18] Pascanuta C, Dragoeb N and Bertheta P 2006 *J. Magn. Magn. Mater.* **305** 6
[19] Rajamani A, Dionne G F, Bono D and Ross C A 2005 *J. Appl. Phys.* **98** 063907
[20] Tan B J, Klabonde K J and Sherwood P M A 1991 *J. Am. Chem. Soc.* **113** 855
[21] Chuang T J, Brundle C R and Rice D W 1976 *Surf. Sci.* **59** 413
[22] Gu Z, Xiang X, Fan G and Li F 2008 *J. Phys. Chem.* C **112** 18459
[23] Petitto S C, Marsh E M, Carson G A and Langell M A 2008 *J. Mol. Catal.* A **281** 49
[24] Nitadori T, Muramatsu M and Misono M 1989 *Chem. Mater.* **1** 215
[25] Perez-Casero R, Perriere J, Gutierrez-Llorente A, Defourneau D, Millon E, Seiler W and Soriano L 2007 *Phys. Rev.* B **75** 165317
[26] Saitoh T, Mizokawa T, Fujimori A, Abbate M, Takeda Y and Takano M 1997 *Phys. Rev.* B **56** 1290

[27] Kaspar T C, Droubay T, Wang C M, Heald S M, Lea A S and Chambers S A 2005 *J. Appl. Phys.* **97** 073511

[28] Yan W *et al* 2009 *Appl. Phys. Lett.* **94** 042508

[29] Janousch M, Meijer G I, Staub U, Delley B, Karg S F and Andreasson B P 2007 *Adv. Mater.* **19** 2232

[30] Cullity B D 1972 *Introduction to Magnetic Materials* (Reading, MA: Addison-Wesley)

[31] Matsui T, Sato R and Tsuda H 2008 *J. Appl. Phys.* **103** 07E304

[32] Ogale S, Kundaliya D, Mehraeen S, Fu L, Zhang S, Lussier A, Dvorak J, Browning N, Idzerda Y and Venkatesan T 2008 *Chem. Mater.* **20** 1344

[33] Kim J Y *et al* 2003 *Phys. Rev. Lett.* **90** 017401

[34] Ballhausen C J 1962 *Introduction to Ligand Field Theory* (New York: McGraw-Hill) chapter 10

[35] Dionne G F 2009 *Magnetic Oxides* (New York: Springer) chapter 6

[36] Dionne G F 1969 *IEEE Trans. Magn.* **5** 596

[37] Dionne G F 1971 *Mater. Res. Bull.* **6** 805

[38] Dionne G F and Kim H S 2008 *J. Appl. Phys.* **103** 07B333

[39] Bi L, Kim H S, Dionne G F, Speakman S A, Bono D and Ross C A 2008 *J. Appl. Phys.* **103** 07D138